



LAWRENCE
LIVERMORE
NATIONAL
LABORATORY

Numerical improvements in magnetohydrodynamic, pulsed power simulations of near-target plasmas

W. A. Farmer, C. L. Ellison, J. H. Hammer, K. R.
LeChien, N. B. Meezan, K. S. Raman, V. Svidzinski, K.
Tummel

September 15, 2023

Institute of Electrical and Electronics Engineers Transactions
on Plasma Science

Disclaimer

This document was prepared as an account of work sponsored by an agency of the United States government. Neither the United States government nor Lawrence Livermore National Security, LLC, nor any of their employees makes any warranty, expressed or implied, or assumes any legal liability or responsibility for the accuracy, completeness, or usefulness of any information, apparatus, product, or process disclosed, or represents that its use would not infringe privately owned rights. Reference herein to any specific commercial product, process, or service by trade name, trademark, manufacturer, or otherwise does not necessarily constitute or imply its endorsement, recommendation, or favoring by the United States government or Lawrence Livermore National Security, LLC. The views and opinions of authors expressed herein do not necessarily state or reflect those of the United States government or Lawrence Livermore National Security, LLC, and shall not be used for advertising or product endorsement purposes.

Numerical improvements in magnetohydrodynamic, pulsed power simulations of near-target plasmas

W. A. Farmer, C. L. Ellison, J. H. Hammer, K. R. LeChien, N. B. Meezan, K. S. Raman, V. Svidzinski, K. Tummel

Abstract—Magnetohydrodynamic (MHD) simulations of pulsed power experiments frequently result in unphysical runaway heating when extended to low values of mass density. Traditionally, this has been addressed by the use of conductivity floors below which the plasma is given an arbitrarily low conductivity value. Here, a low-density treatment is presented that allows for low-density material to carry current while maintaining a stable temperature. This treatment is implemented in the Ares multiphysics code. Numerical modifications to the conventional vacuum treatment include an energy-conserving density floor, a modified averaging procedure to determine the thermal conductivity at the edge of adjacent zones, and a modified averaging procedure for determining the thermal conductivity in mixed zones that contain material from differing regions. Additionally, anomalous resistivity and Bohm diffusion models are implemented as simplified models for microphysics-induced enhancement of collisional transport. The advantage of these various improvements are illustrated in a simple 1D pulsed power target where the combined changes result in stable temperatures within the lower density regions.

I. INTRODUCTION

Pulsed power experiments have significantly enhanced the ability to probe and understand high-energy density physics regimes. Examples include the measurement of opacities [1], [2], the pursuit of ignition and high fusion gain [3]–[6], the production of bright x-ray sources [7], the study of hydrodynamic instabilities [8], and dynamic material experiments [9]. To create these high-energy density conditions on the Sandia Z machine, current flows from Marx capacitor banks along a set of magnetically insulated transmission lines (MITLs) through a load. Stacks of MITLs are connected through a post-hole convolute; a post connects the anodes through small azimuthally spaced holes in the cathodes. This post-hole convolute radially divides the outer MITL region from the inner MITL region where the current density from each transmission line is combined. It has been observed that continuum emission associated with plasma formation occurs in the post-hole convolute with electron densities exceeding 10^{17} cm^{-3} [10], [11]. This contaminant plasma has been modeled with relativistic particle-in-cell simulations [12]–[14], and mass densities of $3 \times 10^{-7} \text{ g/cm}^3$ (or electron densities of roughly 10^{17} cm^{-3}) are predicted. However, simulations of this type are expensive and not practical for load simulations of the solid-density target region. Mechanisms for the generation of this contaminant plasma include space-charge limited emission, water desorption, and the evaporation of metallic surfaces.

Modeling the volume adjacent to the load in radiation-hydrodynamic simulations is challenging due to non-fluid

effects introduced by low-density plasma sourced from the MITLs. This plasma is swept toward the load with the power flow where it can deposit energy and influence magnetic field diffusion into the imploding target. Because there is minimal experimental data on the near-target vacuum conditions of high-current Z facility shots, kinetic simulations of inner MITL power flow can provide the best descriptions of these contaminants [14]. Including plasma in MHD simulations at the conditions given by the kinetic simulations in a fluid target simulation requires a reasonable estimate of the electrical conductivity. In a conventional vacuum treatment, the background is simply modeled as resistive through the use of a density threshold, ignoring the presence of the plasma altogether. Ablated metal that falls below this threshold will also become unphysically infinitely resistive. In reality, the plasma sourced from the MITLs and the ablated metal near the load will spread the current over a larger volume, reducing drive and compression. If the low density material is instead treated as a classical plasma [15], the electrical conductivity is unphysically large and a dramatic current response will be induced, shielding the load almost entirely. In the low-density limit, microinstabilities will occur and correspondingly limit the magnitude of the drift velocity to be on the order of either the ion or electron thermal velocities. These microinstabilities drive small-scale turbulent fluctuations from which electrons will scatter, enhancing the effective collisionality of the plasma and leading to an anomalously high resistivity that reduces currents. In early theta-pinch work, several of these instabilities were considered such as the Buneman, ion acoustic, lower-hybrid-drift, electromagnetic ion cyclotron and ion cross-field instabilities as outlined in the review article of Davidson and Krall [16]. Further work used models of a subset of these instabilities to determine the anomalous transport coefficients, and the fluid equations were numerically solved with these modified coefficients [17], [18]. These simulations matched the gross behavior observed in these early experiments. The inclusion of anomalous resistivity into a fluid code was later used to model fiber Z pinches [19], and most recently to obtain agreement between simulation and measurement of a laser-produced plasma plume expanding in a 20 T magnetic field [20].

Another approach resulting in enhanced diffusion of the magnetic field includes the Hall term in a generalized Ohm's law,

$$\mathbf{E}' = \eta \mathbf{j} + \frac{\mathbf{j} \times \mathbf{B}}{en_e c}, \quad (1)$$

where \mathbf{E}' is the electric field in the frame moving with the ion flow, η , the plasma resistivity, e , the elementary

electric charge, n_e , the electron number density, and c , the speed of light. From the above equation, it is clear that as the electron density vanishes, the current density orthogonal to the magnetic field must also vanish so that the electric field remains finite. Inclusion of Hall physics into a resistive magnetohydrodynamic (MHD) simulation is fraught with both numerical difficulty and the possibility that terms present in a two-fluid treatment are also necessary [21]. One approach to Hall-MHD adopted by the Perseus code involves implementing a relaxation model that includes the Hall term, displacement current, and electron inertia [22]. In magnetized liner inertial fusion (MagLIF) experiments, a helical structure was observed in a partially imploded liner that could not be reproduced using the MHD Gorgon code without introducing an unrealistically large helical perturbation [23], [24]. Hall-MHD simulations with the Perseus code could reproduce the helical structure without a helical perturbation by allowing the plasma around the liner to carry current and compress the preimposed axial field [25]. These simulations were also able to reproduce the helical structure with traditional MHD simulations, but the simulations encountered a serious thermal runaway instability when the plasma density was too low. To obtain stable behavior, they defined a buffer region above the floor density within which the plasma current was zeroed. While this prevented a runaway temperature, it is not a satisfying physical treatment for the low-density plasma near the density floor. In multi-component single-fluid MHD codes often used in integrated design work, we have observed similar behavior: the vacuum tends to over-heat, the conditions are sensitive to a multi-material treatment, and the long mean-free-path of the electrons leads to the conclusion that the classical transport coefficients are invalid.

To address this problem, this paper presents an alternative treatment for low-density plasmas in resistive MHD simulations that does not exhibit spurious heating. This treatment would enable the coupling of a kinetic model of the MITLs with a single-fluid treatment of the load through the use of a mass-flux source as described in [14]. This code coupling is beyond the scope of this work, but the removal of the spurious heating enables such a coupling to be performed. The general approach is to address the most prominent pathologies that emerge when taking the low density, high temperature, magnetized limit of a single-fluid MHD model. Issues can arise in the physics models being used, the numerical discretization of the equations, and the treatment of multimaterial effects. Specifically, the proposed modifications include implementing an energy-conserving density floor, careful definition of the boundary conditions, and modifying the averaging of thermal conductivity near interfaces and in mixed zones. Further, some combination of anomalous resistivity [26], [27] and Bohm diffusion are necessary to enhance magnetic diffusion beyond the classical prediction. These modifications result in and better behavior of the plasma conditions in the low-density regime. We further illustrate the impact of these changes in a test problem utilizing a 1D description of a notional MagLIF-like liner [28] with the hydrodynamics frozen to isolate the evolution of both heat and magnetic field. When all of the modifications are included, the low density plasma is well

behaved and the magnetic field diffuses in a reasonable way. This paper is organized as follows. Background information on the Ares multiphysics code is presented in Sec. II. The alternative low-density plasma treatment is presented in Sec. III. The test problem is defined and the impact of the plasma treatment is shown in in Sec. IV. Finally, major conclusions are summarized in Sec. V.

II. BACKGROUND

Ares is a multiphysics code that has been used in the model and design of various high-energy-density experiments[29]–[31] and physics studies[32]–[34]. In the Ares simulations presented here, the resistive MHD equations are solved,

$$\rho \frac{\partial \rho}{\partial t} + \nabla \cdot (\rho \mathbf{v}) = 0, \quad (2)$$

$$\frac{\partial}{\partial t} (\rho \mathbf{v}) + \nabla \cdot \left[\rho \mathbf{v} \mathbf{v} - \frac{\mathbf{B} \mathbf{B}}{4\pi} + \mathbb{I} \left(p + \frac{B^2}{8\pi} \right) \right] = 0, \quad (3)$$

$$\frac{\partial \mathbf{B}}{\partial t} - \nabla \times (\mathbf{v} \times \mathbf{B}) = -\nabla \times \left(\frac{c^2 \eta}{4\pi} \nabla \times \mathbf{B} \right), \quad (4)$$

where ρ , \mathbf{v} , \mathbf{B} , p , and η are the mass density, the flow velocity, the magnetic field, the total pressure, and the resistivity, respectively, and \mathbb{I} is the rank two identity tensor. The electric field is eliminated from Faraday's law in Eq. (4) with an Ohm's law which includes the dynamo and resistive terms. The pressure gradient term in Ohm's law is ignored because the majority of our application is low plasma β . The thermo-electric term is also ignored due to it contributing only through weak gradients in the coefficient itself. Consideration of the Hall term is outside the scope of this work. The inclusion of anomalous resistivity potentially reduces the importance of the Hall term, and this is discussed more in Sec. V. Finally, the electron inertia or acceleration term is ignored because the electron velocity equilibrates on time scales much faster than the problem, consistent with the MHD approximation. A three temperature model is typically used for integrated simulations with different energy equations for the electrons, ions, and radiation field. Here, we ignore the radiation coupling terms. Then, the total pressure is simply the sum of the electron and ion pressures, $p = p_e + p_i$. The electron and ion energy equations are given by

$$\rho \frac{d\epsilon_e}{dt} + p_e \nabla \cdot \mathbf{v} = \eta j^2 - Q_i + \rho \frac{c_{ve}}{\tau_{ei}^\epsilon} (T_i - T_e) - \nabla \cdot \mathbf{q}, \quad (5)$$

$$\rho \frac{d\epsilon_i}{dt} + p_i \nabla \cdot \mathbf{v} = Q_i + \rho \frac{c_{ve}}{\tau_{ei}^\epsilon} (T_e - T_i). \quad (6)$$

Here, ϵ_e and ϵ_i are the specific energies for the electrons and ions, respectively. The pressures and energies for the ions and electrons are given by the equation-of-state (EOS) specified at the beginning of the simulation. The material derivative is given by $d/dt = \partial/\partial t + \mathbf{v} \cdot \nabla$. The total ohmic heat dissipated is ηj^2 . When using anomalous resistivity models, the energy can be partitioned between the ions and the electrons. The heat transferred to the ions via microturbulence is Q_i , and by conservation of energy, $Q_e = \eta j^2 - Q_i$. The next term is the collisional relaxation of the electron and ion temperatures when not in thermal equilibrium with each other with c_{ve} , τ_{ei}^ϵ ,

T_e , and T_i being the specific heat, the electron-ion collision time, and the electron and ion temperatures, respectively. The form of τ_{ei}^ϵ used is given by Brysk [35], though other options are available within Ares [36], [37]. The electron heat flux is given by \mathbf{q} which in the local limit is given by $\mathbf{q} = -\kappa_\perp \nabla T_e$. Because the simulations here are axisymmetric with the magnetic field in the ignorable direction, only the perpendicular component of the thermal conductivity tensor, κ_\perp , is retained. Ion viscosity is not included, but an artificial viscosity is included in the numerical implementation.

Ares solves the single-fluid-velocity, multi-material, multi-component MHD equations using a staggered-mesh arbitrary Lagrangian-Eulerian (ALE) predictor-corrector scheme [38]. In this mesh and in 2D, density, magnetic field, temperature and specific energy are zone-centered variables, while velocity is defined at the nodes of the mesh. This scheme performs a primary Lagrange step with nodes translating with the fluid motion, then performing a secondary relaxation and remap step toward the initial position. This relaxation governs how Eulerian the ALE prescription is with a full relaxation to the initial position representing a purely Eulerian treatment and no relaxation representing a purely Lagrangian treatment. This relaxation requires all mesh variables be interpolated (remapped) from the post-Lagrange mesh to the relaxed mesh using conservative, finite-volume, total variation diminishing flux-limited advection schemes. In remapping the magnetic field, the finite volume advection preserves magnetic flux. Ares evolves a single-fluid velocity with multiple material densities and temperatures present within any multi-material zone. Each material allows for multiple components (EOSs) which are required to be in pressure and temperature equilibrium with the other components within a given material. Ares uses a linear solve process to achieve this pressure and temperature equilibration of a multi-component material zone. Ares handles multiple-material dynamics with a volume-of-fluid approach. A volume fraction, V_i , is assigned to each material present within a given zone. Along with sub-zonal volume, each material can have its own sub-zonal thermodynamic state (density, temperature, and pressure). These sub-zonal quantities are updated through a pressure relaxation process of volume fractions which differs from the pressure and temperature equilibration that occurs between multiple components. For mixed-zone thermal conductivity, the default in Ares uses a volume-fraction-weighted average of the inverse coefficient. This is performed for the thermal conductivity by

$$\frac{1}{\kappa_{\text{eff}}} = \sum_i \frac{V_i^f}{\kappa_i}, \quad (7)$$

where κ_i is the thermal conductivity of constituent i , V_i^f is the corresponding volume fraction, and κ_{eff} is the effective thermal conductivity in that zone.

When the ‘‘vacuum’’ zones within the domain are treated as a conducting plasma, care must be taken when injecting magnetic flux into the interior of the problem to ensure that nonphysical behavior does not occur. The following prescription gives appropriate behavior near the boundary, and violations of this prescription resulted in pathological behavior

in 2D integrated simulations. First, the node at the boundary and the first interior node are set to be purely Eulerian. Next, the outermost nodes are fixed at their initial position, which is equivalent to setting $\mathbf{v} = 0$ at the boundary. In the simulations reported here, the total current through the load is specified in time as a current source. Through Ampère’s law, the magnetic field at the boundary is specified exploiting the axisymmetry to ensure the specified total amount of current is enclosed within the Ampèrian loop whose outer radius intersects the boundary. Additionally, the code allows specifying an arbitrary voltage, which may originate from a driving circuit or a specified function of time, in which case the appropriate amount of magnetic flux is injected in some number of insulating vacuum zones to induce the driving voltage across the simulation domain. Both of these treatments require the zones in which the magnetic flux is specified / injected to be insulating to achieve the desired enclosed current / driving voltage. To ensure this, the conductivity in the boundary zones is set to an arbitrarily low value so that no Ohmic heating occurs there.

III. LOW-DENSITY PLASMA MODEL

A. Floors

In solving the fluid equations, there are two density floors often used in MHD codes that are relevant to this discussion. The first is the minimum density that a zone can have over the course of the simulation, ρ_m . This can be material specific, but in the simulations reported here, every material is set to have the same ρ_m . Second, when ρ falls below the conductivity floor, ρ_σ , the material is treated as vacuum with small conductivity, σ_{vac} , to enhance diffusion of the magnetic field,

$$\sigma = \begin{cases} \sigma_{\text{vac}}, & \rho < \rho_\sigma \\ \sigma, & \text{otherwise} \end{cases}. \quad (8)$$

The purpose of the treatment given here is to permit choosing $\rho_\sigma < \rho_m$ within various regions of the problem so that low-density regions are conducting plasma. When adopting this approach, ρ_σ no longer acts as a density floor with only the mass floor, ρ_m present. Doing this will remove abrupt transitions in the numerical treatment when the density becomes low. The only consideration in lowering ρ_m to arbitrarily low values will be the Courant condition on the time step due to the explicit numerical solution to the momentum equation. This treatment would allow for a mass flux source from the boundary that injects plasma into the simulation domain at densities above the floor. So long as ρ_m is below the mass density of the incoming flow, the floor could potentially no longer affect the dynamics of the problem.

When the mass density of a zone falls below the value, ρ_m , mass is injected into the system. The modified mass of the zone, ρ' , is

$$\rho' = \max(\rho, \rho_m). \quad (9)$$

Injecting mass into a zone without modifying the specific energy has the consequence of increasing the energy within the system: the initial energy density is $\rho\epsilon$, and the modified energy density becomes $\rho'\epsilon$. Adding energy to these specific zones can be particularly problematic for thermal runaway

because the density floor is often encountered while a zone is undergoing a thermal expansion due to being heated in excess of its neighbors. Therefore, respecting the density floor while not aggravating runaway temperatures in low density zones requires modifying the specific energy so that $\rho\epsilon = \rho'\epsilon'$, or

$$\epsilon'_s = \frac{\rho\epsilon_s}{\rho'}, \quad (10)$$

where $s = i, e$ labels the ion or electron species. While the mass will not be conserved by definition of the floor treatment, energy will be. For this reason, we call this an energy-conserving density floor. In effect, this amounts to injecting zero-energy mass to sustain the density floor as opposed to injecting mass of the same temperature of the zone. The corresponding temperature after applying the floors is given by the EOS. We have found this to be beneficial in integrated 2D simulations, though we do not discuss it further here.

B. Anomalous resistivity and heating

The electrical resistivity η is determined by the material model specified by the user for the materials present in the simulation. The material model can be in tabular or analytic form. From the value for the resistivity, a characteristic ion-electron collision time, τ_{ei} , can be determined and is given by

$$\tau_{ei} = \frac{m_e}{\eta e^2 n_e}. \quad (11)$$

To modify the resistivity to account for the possibility of microturbulence, an effective resistivity is defined by

$$\eta_{\text{eff}} = \eta + \eta_{\text{ar}} = \eta(1 + \tau_{ei}\nu_{\text{ar}}). \quad (12)$$

The effective resistivity η_{eff} is then used in place of the material resistivity η in Eqs (4) and (5). Here, η_{ar} is the anomalous resistivity and ν_{ar} is the characteristic scattering frequency of the electrons due to the small scale turbulent fluctuations. In determining the unmodified resistivity, η , electron-neutral collisions are included so that this effective τ_{ei} will remain finite in all cases. To that end, this expression is precisely the electron-ion collision time only when considering ionized plasmas. In situations where the zone represents material that is partially ionized or neutral, $\tau_{ei}\nu_{\text{ar}} \ll 1$ for parameters relevant to current experiments. Many instabilities are known to generate anomalous resistivity. We primarily adopt anomalous resistivity models based on the lower-hybrid drift instability (LHDI) because this resistivity has been validated under experimentally relevant conditions [27], because these modes do not have the restrictions that $ZT_e \gg T_i$ or $J/nev_{te} > 1$ and are thus more broadly active, and because they are very rapidly growing and saturating on timescales relevant to experiments at the Z facility.

For illustration, here and in the following subsections we consider a simplified, static configuration representative of the Z-pinch systems of interest. The configuration is the interface between a 3-mm radius, room temperature, solid density aluminum rod and a 100 eV ($T_e = T_i$), 10^{-6} g/cm³ hydrogen plasma. Further, the rod carries 10 MA of current in its interior, leading to a 6.6 MG azimuthal magnetic field at the interface.

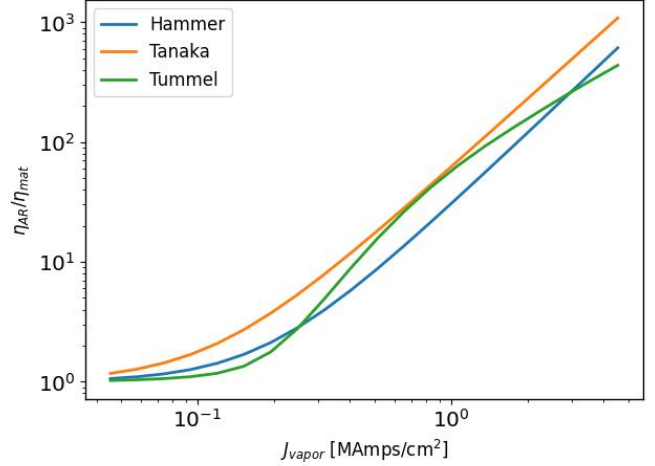


Fig. 1. Anomalous resistivity enhancement (relative to Spitzer resistivity) of a 100 eV, 10^{-6} g/cm³ hydrogen plasma immersed in a 6.6 MG magnetic field for three lower-hybrid instability models described in the text.

Figure 1 shows the effect of including anomalous resistivity in the hydrogen plasma of this test configuration for three different LHDI-based anomalous resistivity models. The three models include the Tummel model [27], a model based on that described by Davidson and Krall [16] (labeled the Hammer model in the figure), and a closely related model presented by Tanaka and Soto [26], with all effective resistivities normalized to the classical Spitzer resistivity. Anomalous resistivity is a strong function of the current density, and here we scan a range of current densities corresponding to 10 kA to 1 MA carried by a 1-mm hydrogen annulus with an inner radius of 3 mm. Clearly, anomalous resistivity has a large effect on such low density plasmas and significantly alters the diffusive evolution of the magnetic field.

When using an anomalous resistivity model, Ohmic heating should no longer be deposited solely into the electrons, and is instead partitioned with the electron and ion heating defined as Q_e and Q_i , respectively. Davidson and Gladd [39] derive expressions for both momentum and energy transfer for the LHDI. These are given in Eqs. (24), (25), and (26) of their manuscript. In the LHDI dispersion relation given by Davidson and Gladd, it is assumed that $|\gamma/\omega| \ll 1$ in the small drift velocity regime, where ω and γ are the real and imaginary part of the complex frequency. Using this approximation, the energy transfer rates can be expressed as,

$$Q_e = \eta j^2 + \eta_{\text{ar}} j^2 \left(1 + \frac{\omega}{ku}\right), \quad (13)$$

$$Q_i = \eta_{\text{ar}} j^2 \left(-\frac{\omega}{ku}\right), \quad (14)$$

where the momentum transfer rate has been related to the anomalous resistivity which contains the same integral expression as the energy transfer equation. The term that accounts for the growth of electric field fluctuations is not included in the heating expressions given above because the LHDI fluctuations are assumed to be in their saturated state. Here, u is the relative drift between the ions and electrons, and the dispersion relation of the LHDI is used to determine ω and

k for the most unstable mode. The full expression requires a sum over the spectrum of unstable LHDI wavelengths, but we approximate this sum by taking ω and k of the fastest-growing modes. An analytic approximation [39] of the dominant LHDI frequency is incorporated into the heating rates to implement this anomalous heating into the fluid simulation,

$$\omega \simeq -\frac{1 + \frac{\omega_{pe}^2}{\Omega_e^2} \left(1 + \frac{ZT_e}{T_i}\right)}{1 + \frac{\omega_{pe}^2}{\Omega_e^2} \left(1 + \frac{2ZT_e}{T_i k^2 \rho_e^2}\right)} k v_{di}, \quad (15)$$

where Z is the charge state of the ions, and ω_{pe} and Ω_e are the electron plasma and cyclotron frequencies, respectively. Here, v_{di} and v_{de} are the respective ion and electron diamagnetic drift velocity as described in Ref. [39], and relate to u through the expression, $u = v_{di} - v_{de} = v_{di}(1 + ZT_e/T_i)$. In Eq. (15), the Bessel function in the electron response is approximated as $I_0(k^2 \rho_e^2/2) \exp(-k^2 \rho_e^2/2) \simeq 1 - k^2 \rho_e^2/2$ with $k \rho_e \simeq 1$ for the dominant modes. Here, ρ_e is the electron Larmor radius. Further, we assume $\omega_{pe}^2/\Omega_e^2 \gg 1$, which for $B \sim 1$ MGauss requires that the electron density satisfy $n_e \gg 10^{17} \text{ cm}^{-3}$, or for a hydrogen plasma $\rho \gg 10^{-7} \text{ g/cm}^3$. For densities below this limit, the resulting expressions for the heating rates will be modified. With these assumptions,

$$\omega \simeq -\frac{1}{1 + 2\tau} k u, \quad (16)$$

with $\tau = ZT_e/T_i$. Incorporating this result into the heating expression yields

$$Q_i = \eta_{ar} j^2 \frac{1}{1 + 2\tau}, \quad (17)$$

$$Q_e = \eta j^2 + \eta_{ar} j^2 \frac{2\tau}{1 + 2\tau}. \quad (18)$$

These expressions are substituted into Eqs. (5) and (6) when using the Tummel model [27] for anomalous resistivity. Figure 2 shows the fraction of Ohmic heat deposited in the ions for the same test configuration used in Fig. 1. At large current densities, 1/3 of the heat is deposited into the ions for this $T_i = T_e$ example. Such an energy partitioning can lead to reduced electron temperatures and less runaway heating, especially given the feedback of the electron temperature on the material resistivity.

C. Bohm Diffusion

In addition to anomalous resistivity, one may include an effective collisional enhancement based on an empirically derived Bohm scaling. It has been observed that in certain systems [40] transport processes exhibit an enhanced collision rate relative to classical magnetized transport theory. To recover the observed scaling, we implement Bohm transport by replacing the collision times in the transport coefficients as:

$$\tau_{ei}^{\text{Bohm}} = \frac{\tau_{ei}}{1 + \Omega_e \tau_{ei}/16} \quad (19)$$

For thermal conduction, in the strongly magnetized limit ($\Omega_e \tau_{ei} \gg 1$) this has the effect of replacing the Braginskii thermal conduction coefficient

$$\kappa_{\perp}^{\text{Braginskii}} \sim \frac{n_e T_e \tau_{ei}}{m_e (\Omega_e \tau_{ei})^2} \quad (20)$$

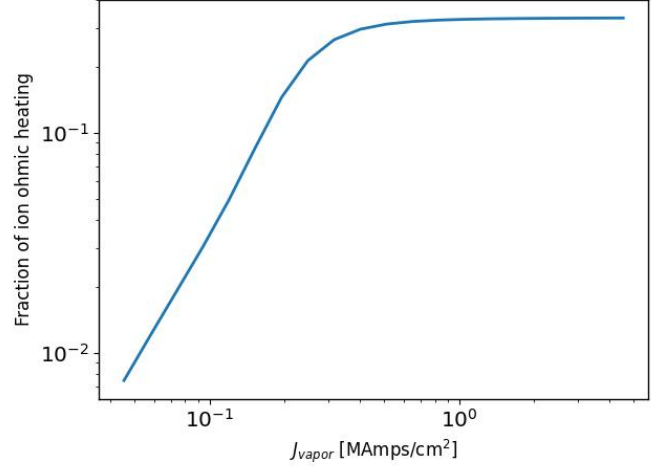


Fig. 2. Fraction of Ohmic heating deposited to ions according to Eq. (18) for a 100 eV, 10^{-6} g/cm^3 hydrogen plasma immersed in a 6.6 MG background magnetic field.

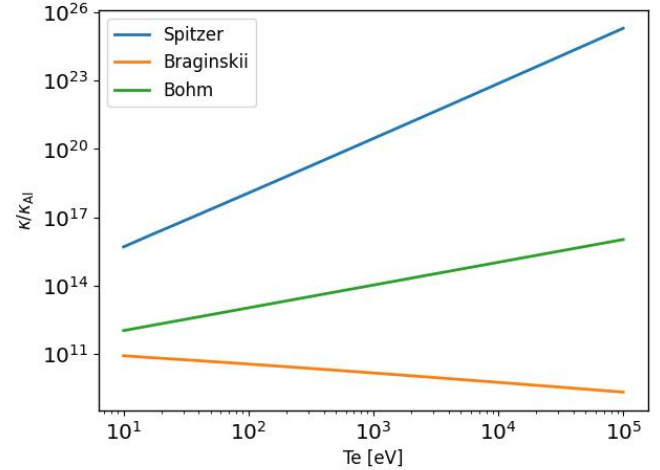


Fig. 3. Magnetized conduction coefficients for a 100 eV, 10^{-6} g/cm^3 hydrogen plasma immersed in a 6.6 MG background magnetic field. Thermal conduction coefficients normalized to room temperature aluminum thermal conductivity $2 \times 10^7 \text{ erg/cm-s-K}$.

with the Bohm thermal conduction coefficient

$$\kappa_{\perp}^{\text{Bohm}} \sim \frac{n_e T_e}{16 m_e \Omega_e}. \quad (21)$$

The modified temperature dependence induced by the Bohm transport scaling has a significant impact on thermal conduction in representative parameters for vacuum contaminant plasmas as shown in Fig. 3. Here we again consider the 10^{-6} g/cm^3 hydrogen test configuration defined in Section III-B to show thermal conduction for Spitzer, Braginskii and Bohm scaling. The Bohm thermal conduction exceeds the Braginskii conduction by factors of 10-1000 at relevant temperatures. Ultimately this has a damping effect on potential runaway heating in the low density region through the significantly enhanced thermal conduction.

In addition to modified thermal conduction, an enhanced effective collision rate would also increase magnetic diffu-

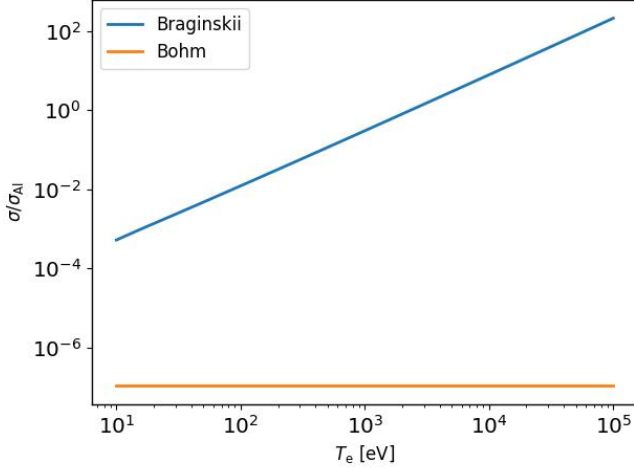


Fig. 4. Electrical conductivity of a 100 eV, 10^{-6} g/cm³ hydrogen plasma immersed in a 6.6 MG background magnetic field using Braginskii and Bohm transport scaling. Conductivities normalized to room temperature aluminum conductivity 3.2×10^{17} s⁻¹.

sivity via the collisional electrical conductivity. In classical Braginskii theory the perpendicular electrical conductivity is only weakly dependent on the level of magnetization $\Omega_e \tau_{ei}$:

$$\sigma_{\perp}^{\text{Braginskii}} = 0.51\sigma_0 = 0.51 \frac{e^2 n_e \tau_{ei}}{m_e} \quad (22)$$

Replacing the classical collision period with the Bohm collision period Eq. (19) yields

$$\sigma_{\perp}^{\text{Bohm}} = 0.51 \frac{e^2 n_e}{16 m_e \Omega_e} \quad (23)$$

so the plasma becomes increasingly resistive with increasing magnetic field strength.

When using tabular models for these transport processes, the collisional enhancement may be incorporated by calculating a representative collision period from the table-defined transport coefficient, e.g.:

$$\tau_{ei}^{\text{tab}} = \frac{\kappa^{\text{tab}} m_e}{n_e T_e} \quad (24)$$

and then proceeding to re-calculate the transport coefficient after modifying the collision period as defined above.

D. Thermal and Electrical Conduction Spatial Discretization

In finite volume schemes like the one employed in Ares, the spatial diffusion of temperature due to thermal conduction requires an evaluation of the heat flux at the face (2D:edge) adjoining two zones. Because the hydrodynamic state variables that the thermal conduction coefficient depends on are known at zone centers, evaluating the heat flux at the face between two zones requires some method of combining the zone-centered thermal conduction coefficients into an effective face-centered conductivity. Standard techniques for calculating such a face-centered average can lead to poor behavior at sharp interfaces (such as the one between a solid density liner and a hot, low-density plasma) even if they are well behaved in

smoothly varying systems. Here we explore one such issue and propose an alternative face-centering interpolation method.

The heat flux is given by $q = -\kappa \nabla T$ with κ having a strong temperature dependence $\kappa = K T_e^p$ for some constant exponent p . The weaker dependencies on charge state and Coulomb logarithm are captured in the coefficient, K . Without loss of generality, we consider a one-dimensional configuration where the x axis is assumed to pass through the two zone centers. With these assumptions, $T_e^p dT_e = -(q/K) dx$. Integrating the right-hand side of this expression through the two zone centers results in, $(\Delta x_1 + \Delta x_2)/K_{\text{edge}} = (\Delta x_1/K_1) + (\Delta x_2/K_2)$. Here $\Delta x_{1,2}$ are the distance from the respective zone center to the edge adjoining the two. Next, the temperature at the edge is computed using the assumed power law for the thermal conductivity. This can be done by finite differencing the relation, $T_e^p = [1/(p+1)](dT_e^{p+1}/dT_e)$. Assuming a $p = 5/2$ Spitzer dependence for the conductivity,

$$K_{\text{edge}} = \frac{\Delta x_1 + \Delta x_2}{(\Delta x_1/K_1) + (\Delta x_2/K_2)}, \quad (25)$$

$$T_{\text{edge}}^{5/2} = \frac{2 T_2^{7/2} - T_1^{7/2}}{7 (T_2 - T_1)} = \frac{2}{7} \sum_{n=0}^6 \frac{T_1^{3-n/2} T_2^{n/2}}{T_1^{1/2} + T_2^{1/2}}, \quad (26)$$

from which the thermal conductivity at the edge is constructed. This interpolation for the thermal conductivity is used in other publications[29]–[31] and is exact in an unmagnetized, fully-ionized, steady-state thermal profile.

The $p = 5/2$ assumption used in the unmagnetized interpolation method is invalid both in the cold, solid-phase liner material and in the strongly magnetized contaminant plasma regions of pulsed power simulations. When calculating the heat flux from the low density plasma to the cold, high density liner, the unmagnetized interpolation scheme yields an effective conductivity that strongly favors the liner's smaller effective K and dramatically reduces the heat flux into the cold material, ultimately leading to runaway heating occurring at interfaces. To fix this problem, we propose implementing a different face-centered averaging procedure. Because this procedure needs to work for all values of the magnetic field that occur throughout the simulation, it is instead assumed that the ionization state of the plasma scales as $\sqrt{T_e}$, reducing the exponent to $p = 2$. In this case,

$$T_{\text{edge}}^2 = \frac{1}{3} (T_1^2 + T_1 T_2 + T_2^2). \quad (27)$$

Further, we construct κ_{edge} via the procedure:

$$\kappa_{\text{edge}} = \frac{1}{3} (\kappa_1 + \sqrt{\kappa_1 \kappa_2} + \kappa_2). \quad (28)$$

This averaging procedure has the consequence that the face-centered coefficient cannot be less than a third of the larger of the two coefficients. Empirically, this procedure behaves well for magnetized plasmas and does not suffer from an unphysical restriction of heat flux when hot, under-dense plasma is adjacent to a cold, dense liner.

Figure 5 compares the effective face-centered thermal conduction coefficient using these two schemes. Here we again consider the static test configuration defined in Section III-B. The 3-mm solid-phase aluminum cylinder is assumed to

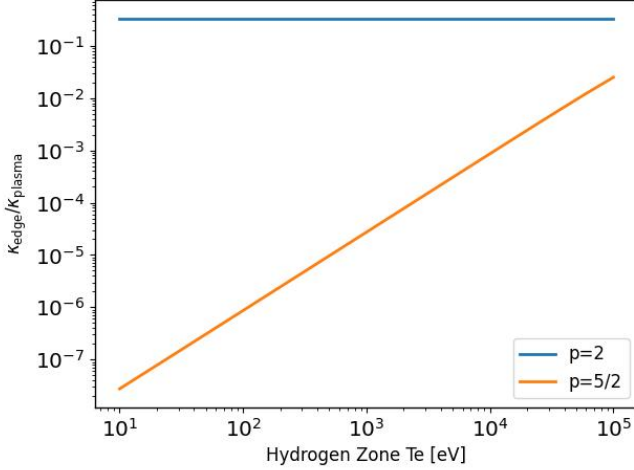


Fig. 5. Edge-based thermal conduction coefficients calculated using the default Ares interpolation method of Eq. (26) and the newly proposed scheme of Eq. (28). One zone is considered to be solid density aluminum at 0.1 eV and a thermal conductivity of 205 W/m K, and the other is 10^{-6} g/cm³ hydrogen in a 6.6 MG magnetic field with Spitzer-Bohm thermal conductivity and temperature given along the x -axis of this figure. The resulting edge-based conduction coefficient is normalized to the thermal conduction coefficient of the hydrogen zone, κ_{plasma} .

have a temperature of 0.1 eV and a thermal conductivity of 205 W/mK. For the hydrogen zone's conductivity, we use the Bohm thermal conductivity of Eqn. (21) The temperature of the hydrogen zone is varied as the independent variable of the figure, revealing the $p = 2$ averaging scheme significantly enhances the effective thermal conductivity relative to the $p = 5/2$ method even up to extremely high temperatures.

The problem of runaway heating of zones adjacent to sharp interfaces between different materials in Ares arises from the discontinuity in resistivity and thermal conduction across the interface. Because the adopted finite difference approximation of the diffusion operator [41] does not separately treat this discontinuity, it introduces a numerical error to $\mathbf{j} = c/4\pi\nabla \times \mathbf{B}$ near the interface, which can cause an overestimate of the Ohmic heating ηj^2 in these zones. The discontinuity in thermal conduction and its ambiguity at the face of the interface can cause significant underestimate of heat flux across the interface, and the zones overheating.

In Ares, the discretization of magnetic diffusion operator in 2D, by analogy with Eq. (25), uses

$$\frac{1}{\sigma_{\text{edge}}} = \frac{\Delta x_1 + \Delta x_2}{\Delta x_1 \sigma_1 + \Delta x_2 \sigma_2}.$$

Ohmic heating uses the edge current, calculated by finite differencing of zone centered magnetic field, and depositing the heating power between adjacent zones as

$$P_1 \propto \frac{\sigma_1 \Delta x_1}{\sigma_1 \Delta x_1 + \sigma_2 \Delta x_2} P_{\text{edge}}, \quad P_{\text{edge}} = \frac{1}{\sigma_{\text{edge}}} j_{\text{edge}}^2$$

Such selective heat deposition reduces heating of a highly resistive zone when it is in contact with a highly conductive zone. Additionally, when density falls below the conductivity floor, ρ_σ , the Ohmic heat is not deposited. This model reduces the possibility of zones overheating in Ares when $\rho > \rho_\sigma$,

but it does not completely eliminate it. One of the goals of this paper is to provide a recipe, based on the physical and numerical arguments presented, which eliminates the nonphysical effect of runaway heating.

E. Multi-material Thermal Conduction

The default averaging process shown in Eq. (7) works well in most cases, and the given expression can be derived assuming a homogeneous plasma mixture and a weakly coupled plasma model for thermal conductivity, i.e., the thermal conductivity is linear with the collision period, so Eq. (7) volume-fraction-averages the collision frequency. In magnetized situations, however, the thermal conductivity is no longer proportional to the collision period, and it can lead to small thermal conduction at the interface between two very different materials where mixed zones contain both low-density and high-density materials. Here, the diffusion model is likely inappropriate, but rather than abandon the diffusion model entirely, minor modifications can be made to enhance the thermal conductivity. Three options were explored. The first is a mass fraction weighted average of the inverse conductivity coefficient,

$$\frac{1}{\kappa_{\text{eff}}} = \sum_i \frac{m_i^f}{\kappa_i}, \quad (29)$$

where m_i^f is the mass fraction of material i present in the zone. The second is a volume-fraction-weighted average of the coefficient,

$$\kappa_{\text{eff}} = \sum_i V_i^f \kappa_i, \quad (30)$$

and the final option, a mass-fraction-weighted average of the coefficient,

$$\kappa_{\text{eff}} = \sum_i m_i^f \kappa_i. \quad (31)$$

The four prospective averaging techniques are compared in Fig. 6 for the test configuration similar to the one defined in Section III-B. Here, instead of considering adjacent non-mixed zones, we examine a single mixed zone containing solid density aluminum and 10^{-6} g/cm³ hydrogen plasma with the volume fraction of the aluminum given by V_{Al}^f . The hydrogen plasma is assumed to have a thermal conduction coefficient 13 orders of magnitude larger, which is reasonable from Fig. 3. The mixture averaging method has a massive impact on the effective conductivity of this zone containing such disparate materials. Both the inverse volume-fraction method of Eq. (7) and the inverse mass-fraction method of Eq. (29) heavily favor the high density, relatively non-conductive aluminum material. The volume-weighted average method of Eq. (30) favors the more highly conducting plasma zone to an extreme degree; so extreme that it is expected to give inaccurate results in mixed zones where the constituents are both in the plasma regime. The direct mass-fraction weighted method of Eq. (31) both maintains a larger conductivity and incorporates the presence of the aluminum to a more significant degree, so we advocate using this method in pulsed power simulations. This method has been found to reduce runaway heating at interfaces and is adopted in the simulations presented in Sec. IV.

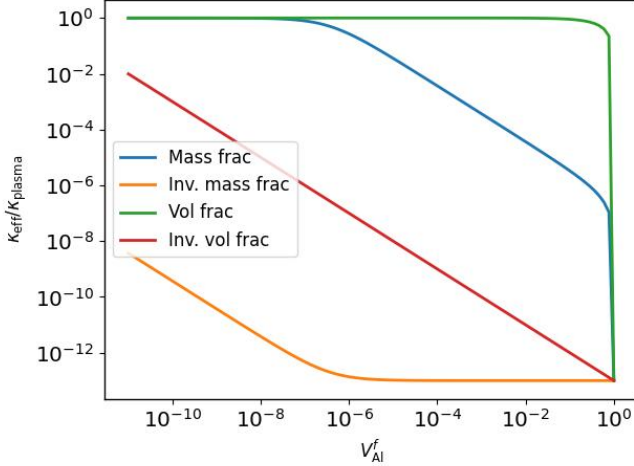


Fig. 6. Effective thermal conductivity in a mixed zone of volume fraction V_{Al}^f of solid-density aluminum and a 10^{-6} g/cm³ hydrogen plasma with thermal conductivity 13 orders of magnitude larger.

IV. RESULTS

The changes are now demonstrated in a simple one-dimensional simulation of a Z-scale MagLIF-like liner implosion. The problem is initialized as shown in Fig. 7 where dimensions have been motivated by Ref. [28]. The gray region shown in the figure is configured with a large, constant vacuum resistivity to allow effectively instantaneous magnetic field diffusion through this layer. The orange, water layer carries current as determined by the physical models chosen. The aluminum and deuterium layers use standard tabular EOS and conductivities used elsewhere [42]. The water is defined using Livermore EOS table 2010 with an analytic four-phase electrical conductivity model [43]. The hydrodynamic motion of the problem is frozen so that the dynamic evolution of the temperature and magnetic field does not depend on the implosion itself. Although hydrodynamic motion of course has a significant impact on the energy balance in actual simulations, removing this potentially confounding factor serves to highlight the influence of the presented vacuum models. The inner most zone of the orange water region is initialized as a mixed zone containing a small amount of aluminum material so that the mixed zone averaging is relevant. In two-dimensional simulations of liner implosions, these mixed zones would typically occur over the course of the problem when mesh motion is not purely Lagrangian. The drive current is given by $I = I_0 \sin^2(t/\tau)$ with $I_0 = 20$ MA and $\tau = 100$ ns. The figures that follow are made at $t = \pi\tau/2$, the time of peak current, so as to show the total heating and magnetic diffusion that has taken place over the course of the problem. Because the motion is frozen, the amount of Ohmic heating is somewhat overstated due to the lack of $\mathbf{E} \times \mathbf{B}$ motion within the simulation, but similar features are observed when performing 2D simulations of experiments performed on Z, e.g., [42]. This problem should exclude current (and Ohmic heating) from the gray region in Fig. 7. In order to prevent runaway heating, the current carried in the orange

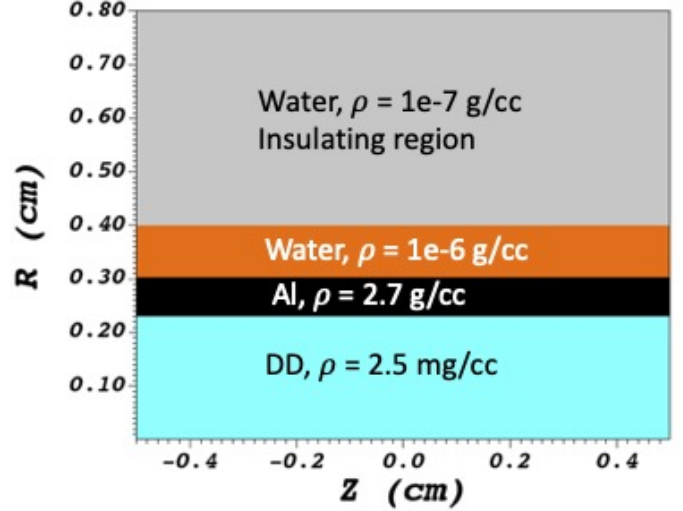


Fig. 7. One-dimensional, MagLIF like simulation setup. The aluminum liner is $70 \mu\text{m}$ thick with a 3 mm outer radius. The orange water layer is 1 mm thick and is present to illustrate the impact of low-density material within the simulation. The gray water layer is initialized as insulating to spatially isolate the runaway heating effects.

region should be modest with heat flux penetrating into the aluminum liner. If Ohmic heating heats the water faster than the heat is carried away, the temperature will runaway.

To illustrate the impact of the model presented in this manuscript, temperature profiles are plotted at the time of peak current as shown in Fig. 8. The baseline case, as shown by the blue curve, uses all of the modifications suggested in this manuscript: the $p = 2$ thermal conduction discretization, the mass-fraction averaging in mixed zones, and the inclusion of an anomalous resistivity model (Tanaka in this case) and Bohm diffusion. In this case, the low density material gets heated to roughly 4 keV. If the $\rho = 10^{-6}$ g/cc water is given an artificially high resistivity, then the orange curve results with little heating occurring in this region. Altering from the baseline settings so that either the $p = 5/2$ temperature discretization or the inverse-volume fraction averaging is used, then the green and red curve result, respectively, with the plasma heating to roughly 70 keV. If the baseline case were simulated with the same settings but with no mixed zone (i.e., the mesh is conformal with the region boundary), the net effect is simply to shift the temperature profile slightly to greater radii. This shift can be understood by viewing the mixed zone as a lack of resolution at an infinitely sharp boundary.

Figure 9 presents a series of runs examining the impact of modeling settings on the magnetic diffusion of the 1-D test problem. The baseline case shown here is the same vacuum settings as those used above, and the magnetic profile for all the cases in Fig. 8 looks nearly identical to the blue curve in Fig. 9. The green and red curves correspond to the respective Tummel and Tanaka anomalous resistivity models without Bohm diffusion. The lack of penetration of the magnetic field below 0.4 cm where the water layer begins illustrates the more conductive nature of the Tummel model as initially shown in Fig. 1. To illustrate the impact of Bohm diffusion, a simulation

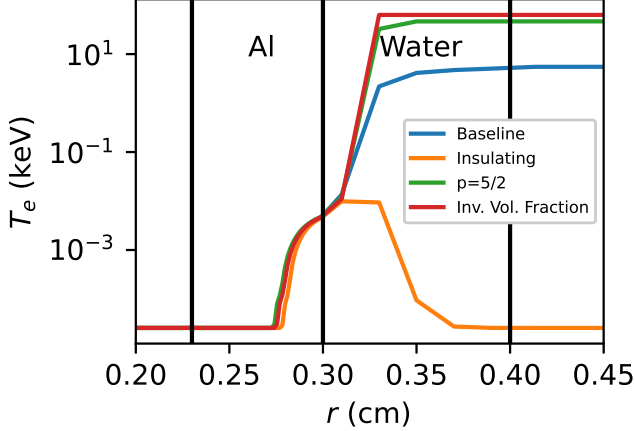


Fig. 8. Temperature versus radius for the simulation defined in Fig. 7. The blue curve includes the low-density treatment suggested here with a Tanaka anomalous resistivity model and Bohm diffusion. The orange curve is the result when the water layer adjacent to the target is not allowed to carry current. Finally, the green and red curves show uncontrolled heating when the respective $p = 5/2$ interpolation model and the inverse volume fraction mixed zone averaging are used.

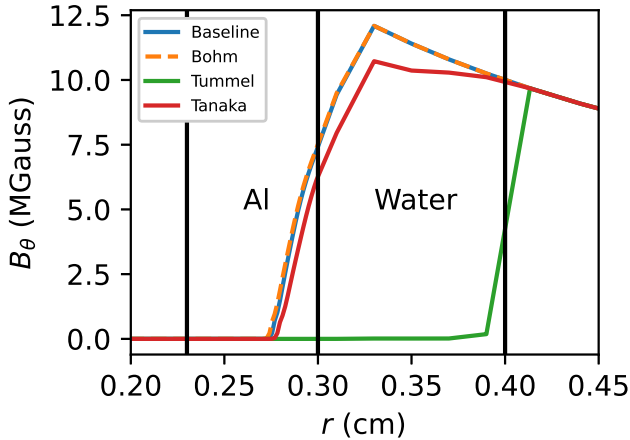


Fig. 9. Magnetic field versus radius for the simulation defined in Fig. 7. All simulations use the prescription to remove runaway heating. The orange and green curves use the Tummel and Tanaka LHDI anomalous resistivity models, respectively. The blue and dashed orange curves use Bohm diffusion with and without the Tanaka model respectively and overlay each other.

is performed with Bohm diffusion but no anomalous resistivity (dashed orange) and with the Tanaka model (blue baseline curve). The magnetic field for these two simulations lie on top of each other, showing the enhancement of magnetic diffusion through the low-density water. When using Bohm diffusion, then, the models will primarily differ in the heating that occurs in the low-density regions. The corresponding temperature profiles are given in Fig. 10. Temperature differences are seen between the different models. These differences are primarily due to differences in magnetic diffusion and the associated Ohmic heating.

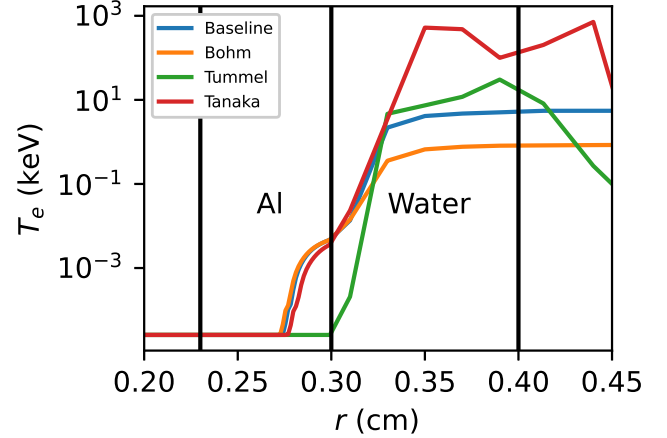


Fig. 10. Temperature versus radius corresponding to the plots shown in Fig. 9. The temperature profile varies for the different cases and is primarily due to differences in magnetic diffusion.

V. DISCUSSION AND CONCLUSION

Here, we present a low-density plasma treatment in a single-fluid radiation-hydrodynamic code that behaves reasonably at low-densities. The essential ingredients of this model include an energy-conserving density floor, an anomalous resistivity treatment, Bohm diffusion, and modifications to how thermal conductivity is determined at interfaces and in mixed-zones. In absolute terms, such modifications will never be able to fully capture kinetic effects that will emerge as the density is extrapolated to zero due to the failure of the fluid approximation altogether. Nevertheless, these limitations may not be important for the dynamic evolution of the load. This treatment could potentially allow for a “floorless” model. In such an approach, a plasma-flux source could be injected from the boundary with conditions determined either via kinetic simulations [12], [13] or from measurement. If the mass-density floor is set such that ρ_m is smaller than the mass of the injected plasma, then due to the cylindrically converging nature of the flows, the density of the injected plasma will stay above ρ_m . In such a situation, the density floors will no longer be dynamically significant.

In situations where there is no low-density plasma surrounding the load and a true vacuum is more appropriate, the standard approach for resistive MHD simulations in the literature is to simply treat that region with a large resistivity when the density falls below some threshold. Depending on the important observables in the experiment, this can potentially work well, e.g. [42]. However, as the metallic surface vaporizes, there is the potential for the resultant plasma to be mixed in with the vacuum region. This could result in highly conducting zones adjacent to highly resistive zones when in reality, the two regions will interpenetrate. Such problems may be overcome through multi-fluid models, but accurately modeling the resistivity and of the plasma will still be important and some of the work presented here may bear on that problem. Fully kinetic modeling would of course address

all of these concerns but is computationally expensive.

This treatment is illustrated in a test problem which contains a low-density conducting layer of water surrounding a MagLIF like load with the motion of the target frozen. In this simple test problem, it is shown that the plasma heats to roughly 70 keV without various ingredients of this approach, whereas, with the modifications, the low density plasma is reduced to roughly 4 keV. Further, it is shown that Bohm diffusion significantly enhances diffusion of the magnetic field beyond predictions made with an anomalous resistivity model. Physically, diffusion of the magnetic field will be primarily dependent on the plasma conditions of the material near the load. This will, of course, be influenced by low-density plasma that is sourced from the post-hole convolute and vaporization of the metallic surfaces of the load itself. This low-density material will rapidly be accelerated to the $\mathbf{E} \times \mathbf{B}$ speed, reducing its ability to carry current, and near the load, it will be compressed to higher densities where the classical predictions are of greater validity. It is impossible to determine the physically correct approach without both experimental measurements characterizing this low-density material and kinetic simulations that provide an a priori way of predicting this plasma.

The proposed low-density treatment raises many questions. First, can this prescription capture the observed helical structure [23], [24] in MagLIF experiments? Since this allows for the low-density plasma to carry current, it should allow low-density plasma to compress the axial magnetic field. Ref. [25] showed that the helical structure can be captured in a resistive MHD treatment but is prone to runaway heating. The low-density model presented here addresses this criticism. Second, to what extent is Hall physics relevant in these pulsed-power plasmas when microinstabilities should enhance resistive diffusion of the magnetic field? The Hall electric field dynamically impacts magnetic diffusion when $\Omega_e \tau_{ei} \gtrsim 1$, where Ω_e is the electron cyclotron frequency. In the presence of enhanced magnetic diffusion due to microinstabilities, the classical electron-ion collision time should no longer be used and should be replaced by $1/\nu_{ar}$ so that the limit is now $\Omega_e/\nu_{ar} \gtrsim 1$. Due to the strong current densities that are driven in pulsed-power systems, it is possible that magnetic diffusion will instead be dominated by microturbulence with $\Omega_e/\nu_{ar} \ll 1$. Finally, while a LHDI anomalous resistivity model is used, it is not clear that this is the appropriate model at all times and for all plasma conditions. Other processes may be present, e.g., the ion-acoustic wave instability and Buneman instability, and the ad hoc inclusion of Bohm diffusion suggests that it is likely that other processes are enhancing diffusion of the magnetic field. Further thought should be given to a unified treatment of these phenomena. These questions are all deferred to future work.

ACKNOWLEDGEMENT

We'd like to thank G. B. Zimmerman for useful discussions. This work was performed under the auspices of the U.S. Department of Energy by Lawrence Livermore National Laboratory under Contract DE-AC52-07NA27344.

The data that support the findings of this study are available from the corresponding author upon reasonable request.

REFERENCES

- [1] P. T. Springer, K. L. Wong, C. A. Iglesias, J. H. Hammer, J. L. Porter, A. Toor, W. H. Goldstein, B. G. Wilson, F. J. Rogers, C. Deeney, D. S. Dearborn, C. Bruns, J. Emig, and R. E. Stewart, "Laboratory measurement of opacity for stellar envelopes," *J. Quant. Spectrosc. Radiat. Transf.*, vol. 58, no. 4, pp. 927–935, 1997.
- [2] J. E. Bailey, T. Nagayama, G. P. Loisel, G. A. Rochau, C. Blancard, J. Colgan, P. Cosse, G. Faussurier, C. J. Fontes, F. Gilleron, I. Golovkin, S. B. Hansen, C. A. Iglesias, D. P. Kilcrease, J. J. MacFarlane, R. C. Mancini, S. N. Nahar, C. Orban, J.-C. Pain, A. K. Pradhan, M. Sherrill, and B. G. Wilson, "A higher-than-predicted measurement of iron opacity at solar interior temperatures," *Nature*, vol. 517, no. 7532, pp. 56–59, 2015.
- [3] S. A. Slutz, M. C. Herrmann, R. A. Vesey, A. B. Sefkow, D. B. Sinars, D. C. Rovang, J. J. Peterson, and M. E. Cuneo, "Pulsed-power-driven cylindrical liner implosions of laser preheated fuel magnetized with an axial field," *Phys. Plasmas*, vol. 17, p. 056303, 2010.
- [4] S. A. Slutz and R. A. Vesey, "High-gain magnetized inertial fusion," *Phys. Rev. Lett.*, vol. 108, no. 2, p. 025003, 2012.
- [5] T. W. L. Sanford, R. E. Olson, R. L. Bowers, G. A. Chandler, M. S. Derzon, D. E. Hebron, R. J. Leeper, R. C. Mock, T. J. Nash, D. L. Peterson, L. E. Ruggles, W. W. Simpson, K. W. Struve, and R. A. Vesey, "Z-pinch generated x-rays demonstrate potential for indirect-drive icf experiments," *Phys. Rev. Lett.*, vol. 83, no. 26, p. 5511, 1999.
- [6] R. E. Olson, G. A. Chandler, M. S. Derzon, D. E. Hebron, J. S. Lash, R. J. Leeper, T. J. Nash, G. E. Rochau, T. W. L. Sanford, N. B. Alexander, and C. R. Gibson, "Indirect-drive icf target concepts for the x-1 z-pinch facility," *Fusion Tech.*, vol. 35, no. 2, pp. 260–265, 1999.
- [7] M. K. Matzen, "Z pinches as intense x-ray sources for high-energy density physics applications," *Phys. Plasmas*, vol. 4, no. 5, p. 1519, 1997.
- [8] D. B. Sinars, S. A. Slutz, M. C. Herrmann, R. D. McBride, M. E. Cuneo, K. J. Peterson, R. A. Vesey, C. Nakhleh, B. E. Blue, K. Killebrew, D. Schroen, K. Tomlinson, A. D. Edens, M. R. Lopez, I. C. Smith, J. Shores, V. Bigman, G. R. Bennett, B. W. Atherton, M. Savage, W. A. Stygar, G. T. Leifeste, and J. L. Porter, "Measurements of magneto-rayleigh-taylor instability growth during the implosion of initially solid al tubes driven by the 20-ma 100-ns z facility," *Phys. Rev. Lett.*, vol. 105, p. 185001, 2010.
- [9] D. C. Swift, T. E. Tierney, S.-N. Luo, D. L. Paisley, G. A. Kyrala, A. Hauer, S. R. Greenfield, A. C. Koskelo, K. J. McClellan, H. E. Lorenzana, D. Kalantar, B. A. Remington, P. Peralta, and E. Loomis, "Dynamic response of materials on subnanosecond time scales, and beryllium properties for inertial confinement fusion," *Phys. Plasmas*, vol. 12, p. 056308, 2005.
- [10] A. Porwitzky, D. H. Dolan, M. R. Martin, G. Laity, R. W. Lemke, and T. R. Mattsson, "Direct measurements of anode/cathode gap plasma in cylindrically imploding loads on the z machine," *Phys. Plasmas*, vol. 25, p. 063110, 2018.
- [11] M. R. Gomez, R. M. Gilgenbach, M. E. Cuneo, C. A. Jennings, R. D. McBride, E. M. Waisman, B. T. Hutsel, W. A. Stygar, D. V. Rose, and Y. Maron, "Experimental study of current loss and plasma formation in the z machine post-hole convolute," *Phys. Rev. Accel. Beams*, vol. 20, p. 010401, 2017.
- [12] D. V. Rose, D. R. Welch, T. P. Hughes, R. E. Clark, and W. A. Stygar, "Plasma evolution and dynamics in high-power vacuum-transmission-line post-hole convolutes," *Phys. Rev. Accel. Beams*, vol. 11, p. 060401, 2008.
- [13] D. R. Welch, N. Bennett, T. C. Genoni, D. V. Rose, C. Thoma, C. Miller, and W. A. Stygar, "Electrode contaminant plasma effects in 10^7 -a z pinch accelerators," *Phys. Rev. Accel. Beams*, vol. 22, p. 070401, 2019.
- [14] K. Tummel, D. R. Welch, D. V. Rose, A. J. Link, and K. R. LeChien, "Impact of power flow on z-pinch loads," *Phys. Plasmas*, vol. 29, p. 113102, 2022.
- [15] S. I. Braginskii, *Transport processes in a plasma*. Consultants Bureau, New York, 1965, vol. 1, pp. 205–311.
- [16] R. C. Davidson and N. A. Krall, "Anomalous transport in high-temperature plasma with applications to solenoidal fusion systems," *Nucl. Fusion*, vol. 17, no. 6, pp. 1313–1372, 1977.
- [17] P. C. Liewer and N. A. Krall, "Self-consistent approach to anomalous resistivity applied to theta pinch experiments," *Phys. Fluids*, vol. 16, no. 11, pp. 1953–1963, 1973.

- [18] —, “Anomalous penetration of a magnetic pulse into a plasma,” *Phys. Rev. Lett.*, vol. 30, no. 25, pp. 1242–1245, 1973.
- [19] J. P. Chittendon, “The effect of lower hybrid instabilities on plasma confinement in fiber z pinches,” *Phys. Plasmas*, vol. 2, p. 1242, 1995.
- [20] B. Khair, G. Revet, A. Ciardi, K. Burdonov, E. Filippov, J. Béard, M. Cerchez, S. N. Chen, T. Gangolf, S. S. Makarov, M. Ouillé, M. Safranov, I. Y. Skobolev, A. Soloviev, M. Starodubtsev, O. Willi, S. Pikuz, and J. Fuchs, “Laser-produced magnetic-rayleigh-taylor unstable plasma slabs in a 20 t magnetic field,” *Phys. Rev. Lett.*, vol. 123, p. 205001, 2019.
- [21] B. Srinivasan and U. Shumlak, “Analytical and computational study of the ideal full two-fluid plasma model and asymptotic approximations for hall-magnetohydrodynamics,” *Phys. Plasmas*, vol. 18, p. 092113, 2011.
- [22] C. E. Seyler and M. R. Martin, “Relaxation model for extended magnetohydrodynamics: Comparison to magnetohydrodynamics for dense z-pinches,” *Phys. Plasmas*, vol. 18, no. 1, p. 012703, 2011.
- [23] T. J. Awe, R. D. McBride, C. A. Jennings, D. C. Lamppa, M. R. Martin, D. C. Rovang, S. A. Slutz, M. E. Cuneo, A. C. Owen, D. B. Sinars, K. Tomlinson, M. R. Gomez, S. B. Hansen, M. C. Herrmann, J. L. McKenney, C. Nakhleh, G. K. Robertson, G. A. Rochau, M. E. Savage, D. G. Schroen, and W. A. Stygar, “Observations of modified three-dimensional instability structure for imploding z-pinch liners that are premagnetized with an axial field,” *Phys. Rev. Lett.*, vol. 111, p. 235005, 2013.
- [24] T. J. Awe, C. A. Jennings, R. D. McBride, M. E. Cuneo, D. C. Lamppa, M. R. Martin, D. C. Rovang, D. B. Sinars, S. A. Slutz, A. C. Owen, K. Tomlinson, M. R. Gomez, S. B. Hansen, M. C. Herrmann, M. C. Jones, J. L. McKenney, G. K. Robertson, G. A. Rochau, M. E. Savage, D. G. Schroen, and W. A. Stygar, “Modified helix-like instability structure on imploding z-pinch liners that are pre-imposed with a uniform axial magnetic field,” *Phys. Plasmas*, vol. 21, p. 056303, 2014.
- [25] C. E. Seyler, M. R. Martin, and N. D. Hamlin, “Helical instability in maglif due to axial flux compression by low-density plasma,” *Phys. Plasmas*, vol. 25, no. 6, p. 062711, 2018.
- [26] M. Tanaka and T. Sato, “Simulations on lower hybrid drift instability and anomalous resistivity ion the magnetic neutral sheet,” *J. Geophys. Res.*, vol. 86, no. A7, p. 5541, 1981.
- [27] K. Tummel, C. L. Ellison, W. A. Farmer, J. H. Hammer, J. B. Parker, and K. R. LeChien, “Kinetic simulations of anomalous resistivity in high-temperature current carrying plasmas,” *Phys. Plasmas*, vol. 27, p. 092306, 2020.
- [28] D. E. Ruiz, P. F. Schmit, D. A. Yager-Elorriaga, M. R. Gomez, M. R. Weiss, C. A. Jennings, A. J. Harvey-Thompson, P. F. Knapp, S. A. Slutz, D. J. Ampleford, K. Beckwith, and M. K. Matzen, “Exploring the parameter space of maglif implosions using similarity scaling. ii. current scaling,” *Phys. Plasmas*, vol. 30, p. 032708, 2023.
- [29] C. L. Ellison, H. D. Whitley, C. R. D. Brown, S. R. Copeland, W. J. Garbett, H. P. Le, M. B. Schneider, Z. B. Walters, H. Chen, J. I. Castor, R. S. Craxton, M. Gatu Johnson, E. M. Garcia, F. R. Graziani, G. E. Kemp, C. M. Krauland, P. W. McKenty, B. Lahmann, J. E. Pino, M. S. Rubery, H. A. Scott, R. Shepherd, and H. Sio, “Development and modeling of a polar-direct-drive exploding pusher platform at the national ignition facility,” *Phys. Plasmas*, vol. 25, no. 7, p. 072710, 2018.
- [30] J. D. Bender, O. Schilling, K. S. Raman, R. A. Mannagan, B. J. Olson, S. R. Copeland, C. L. Ellison, D. J. Erskine, C. M. Huntington, B. E. Morgan, S. R. Nagel, S. T. Prisbrey, B. S. Pudliner, P. A. Sterne, C. E. Wehrenberg, and Y. Zhou, “Simulation and flow physics of a shocked and reshocked high-energy-density mixing layer,” *J. Fluid Mech.*, vol. 915, p. A84, 2021.
- [31] H. D. Whitley, G. E. Kemp, C. B. Yeaman, Z. B. Walters, B. E. Blue, W. J. Garbett, M. B. Schneider, R. S. Craxton, E. M. Garcia, P. W. McKenty, M. Gatu-Johnson, K. Caspersen, J. I. Castor, M. Dane, C. L. Ellison, J. A. Gaffney, F. R. Graziani, J. E. Klepeis, N. B. Kostinski, A. L. Kritcher, B. Lahmann, A. E. Lazicki, H. P. Le, R. A. London, B. Maddox, M. C. Marshall, M. E. Martin, B. Militzer, A. Nikroo, J. Nilsen, T. Ogitsu, J. E. Pask, J. E. Pino, M. S. Rubery, R. Shepherd, P. A. Sterne, D. C. Swift, L. Yang, and S. Zhang, “Comparison of ablaters for the polar direct drive exploding pusher platform,” *High Energy Density Phys.*, vol. 38, p. 100928, 2021.
- [32] W. A. Farmer, C. L. Ellison, and J. H. Hammer, “Linear response of a hall magnetic drift wave for verification of hall mhd algorithms,” *Phys. Plasmas*, vol. 26, p. 072120, 2019.
- [33] R. L. Masti, C. L. Ellison, J. R. King, P. H. Stoltz, and B. Srinivasan, “Cross-code verification and sensitivity analysis to effectively model the electrothermal instability,” *High Energy Density Phys.*, vol. 38, p. 100925, 2021.
- [34] R. L. Masti, C. L. Ellison, W. A. Farmer, K. Tummel, and B. Srinivasan, “The effect of anomalous resistivity on fast electrothermal instability,” *Phys. Plasmas*, vol. 28, p. 102106, 2021.
- [35] H. Brysk, “Electron-ion equilibration in a partially degenerate plasma,” *Plasma Phys.*, vol. 16, pp. 927–932, 1974.
- [36] S. D. Bergeson, S. D. Baalrud, C. L. Ellison, E. Grant, F. R. Graziani, T. C. Killian, M. S. Murillo, J. L. Roberts, and L. G. Stanton, “Exploring the crossover between high-energy-density plasma and ultracold neutral plasma physics,” *Phys. Plasmas*, vol. 26, p. 100501, 2019.
- [37] C. R. Scullard, S. Serna, L. X. Benedict, C. L. Ellison, and F. R. Graziani, “Analytic expressions for electron-ion temperature equilibration rates from the lenard-balescu equation,” *Phys. Rev. E*, vol. 97, p. 013205, 2018.
- [38] R. M. Darlington, T. L. McAbee, and G. Rodrigue, “A study of ale simulations of rayleigh-taylor instability,” *Comput. Phys. Commun.*, vol. 135, no. 1, pp. 58–73, 2001.
- [39] R. C. Davidson and N. T. Gladd, “Anomalous transport properties associated with the lower-hybrid-drift instability,” *Phys. Fluids*, vol. 18, p. 1327, 1975.
- [40] D. Bohm, E. H. S. Burhop, and H. S. W. Massey, *The Characteristics of Electrical Discharges in Magnetic Fields*. New York: McGraw-Hill, 1949, ch. The use of probes for plasma exploration in strong magnetic fields, pp. 13 – 76.
- [41] G. Pert, “Physical constraints in numerical calculations of diffusion,” *J. Comput. Phys.*, vol. 42, no. 1, pp. 20 – 52, 1981. [Online]. Available: <http://www.sciencedirect.com/science/article/pii/002199918190231X>
- [42] C. E. Myers, D. E. Bliss, P. M. Celliers, P. S. Datte, M. H. Hess, C. A. Jennings, M. C. Jones *et al.*, “Radially resolved measurements of load current delivery on a 14 ma, 100 ns pulsed power experiment using a line-imaging velocity interferometer,” *Phys. Rev. Accel. Beams*, vol. 26, no. 7, p. 070401, 2023.
- [43] T. J. Burgess, “Electrical resistivity model of metals,” in *Megagauss Technology and Pulsed Power Applications*, C. M. Fowler, R. S. Caird, and D. J. Erickson, Eds. Plenum Press, July 1986, pp. 307–316.